European Journal of Mechanics / A Solids 85 (2021) 104149

Contents lists available at ScienceDirect

European Journal of Mechanics / A Solids

journal homepage: www.elsevier.com/locate/ejmsol

First observation of spalling in tantalum at high temperatures induced by high energy proton beam impacts

Claudio Torregrosa Martin [a,*], Nicola Solieri [a], Elvis Fornasiere [b,a], Josep Busom Descarrega [a], Marco Calviani [a], Joao Canhoto Espadanal [a], Antonio Perillo-Marcone [a], Philippe Spätig [b,c]

[a] European Laboratory for Particle Physics (CERN), 1211, Geneva 23, Switzerland
[b] Laboratory for Reactor Physics and Systems Behaviour, Ecole Polytechnique Federale de Lausanne, 1015 Lausanne, Switzerland
[c] Laboratory for Nuclear Materials, Paul Scherrer Institute, 5232 Villigen, Switzerland

ARTICLE INFO

Keywords:
Spall
Tantalum
High temperature
Proton beams
Dynamic loading
Radial mode
Hydrocodes

ABSTRACT

Spalling in tantalum has been observed in an experiment aiming at testing an antiproton production target prototype at CERN's HiRadMat Facility. The experiment consisted in impacting 47 intense and high-energy proton beams onto a target equipped with ten cylindrical cores made of tantalum of Ø8 mm by 16 mm. Each of these proton beam impacts induced a sudden rise of temperature in the bulk of the Ta cores around 1800 °C in 0.9 μs leading to the excitation of a vibration mode which exposed their material to compressive-to-tensile pressures ranging from 2 GPa to 9 GPa, with pressure rates up to 20 GPa/μs. Post-irradiation analyses such as neutron tomography and metallographic examination of the cores, revealed the creation of voids in the bulk of the tantalum cores ranging from to 2 μm to 1 mm in diameter. These voids present a non-uniform size and density distribution within the cores, with limited growth and coalescence in areas subjected to higher temperatures and tensile pressures. Grain-growth due to a fast, thermally-induced, recrystallization has been also observed in some zones. In this work, we present a detailed characterization of the unique thermal and mechanical load that has induced this spall process by means of Finite Element and hydrocode simulations, together with post-experiment microscope and EBSD observations of the Ta rods. This analysis suggests that spall-induced void growth and coalescence is enhanced in the temperature and pressure window of 1300-1800 °C and 3-6.5 GPa, whereas is restrained at temperatures and tensile pressures above 2000 °C and 6.5 GPa. In addition, the analysis suggests that full thermal-recrystallization in tantalum can take place when exposed to temperatures above 2000 °C for less than 2 s. Four different hypotheses to explain the observed void size distribution trends are presented.

1. Introduction

The present study deals with the appearance of voids observed in the bulk of tantalum rods after exposing them to high dynamic stresses induced by high-energy proton beam impacts. Interest on the response of refractory metals exposed to high dynamic loading started recently at the European Laboratory for Particle Physics (CERN) in the context of the design and manufacturing of a new generation of antiproton production targets (AD-Target). For antiproton production, intense and short 26 GeV/c momentum proton beams are impacted within the axis of thin rods of 3–10 mm in diameter and 5–7 cm long. These rods, called "target cores", shall be made of a high density material (for physics reasons), such as iridium, tungsten or tantalum. Differently from ion beams or lasers, relativistic proton beams can easily penetrate several centimetres (or tens of centimetres) of high density metals. Therefore, the incident proton beams induces a sudden deposition of energy in the bulk of the target rods, leading to a fast temperature rise and subsequent dynamic stresses. This phenomenon was studied numerically in Ref. Torregrosa et al. (2016) using the hydrocode AUTODYN®, finding that a temperature rise of the order of 2000 °C takes place in every proton beam impact, which has a duration of 0.4 μs. This fast thermal load induces the excitation of several vibrations modes, dominated by a high frequency radial one which exposes the target material to compression-to-tension oscillating pressures of several GPas, leading to plastic deformation and eventual failure.

In this same context, several experiments have been performed using the CERN's HiRadMat facility (Efthymiopoulos et al., 2011). This facility is designed to test accelerator components by providing

* Corresponding author.
E-mail address: claudio.torregrosa@cern.ch (C. Torregrosa Martin).

https://doi.org/10.1016/j.euromechsol.2020.104149
Received 18 December 2019; Received in revised form 11 September 2020; Accepted 20 October 2020
Available online 22 October 2020

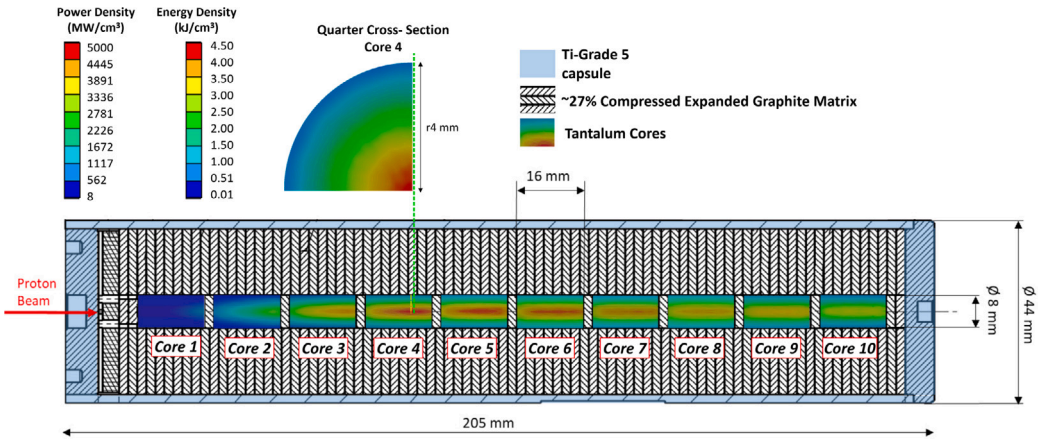

Fig. 1. Schematic representation of the HRMT-42 target, equipped with ten tantalum cores of Ø8 mm by 16 mm, onto which 47x high energy proton beams were impacted.

intense and fast extracted 440 GeV/c proton beams to an experimental area. The first of these experiment related to high-density materials for antiproton production was the so called HRMT-27 experiment (Torregrosa et al., 2019b), in which dynamic conditions equivalent to the ones taking place in the AD-Target were recreated within different refractory metals, candidate materials for the new design, such as iridium, tungsten, molybdenum, TZM alloy and tantalum. The recorded surface velocity of the targets after each proton impact was used to validate the predictions of the hydrocode simulations. In addition, it was found that all the tested materials except tantalum suffered from internal brittle fracture at conditions 7 to 5 times less extreme than the ones taking place in the AD-Target (in terms of temperature rise and tensile pressures). Tantalum targets on the other hand, behaved apparently surprisingly well, withstanding AD-Target conditions without fracturing, only experiencing plastic deformation. This result motivated the execution of a second experiment, so-called HRMT-42, in which a scaled prototype of the new AD-Target design as shown in Fig. 1, was exposed to 47 proton pulses at the HiRadMat facility, reaching equivalent AD-Target conditions in each of the these pulses (in the previous HRMT-27 experiment only one high intensity pulse was impacted in Tantalum).

Fig. 1 shows the geometry of the HRMT-42 target, which has a core made of ten rods of tantalum of Ø 8 mm by 16 mm in length. These tantalum rods were manufactured out of melted material ingots, hammered, grounded, and delivered in non-annealed conditions by PLANSEE (Obererlacher, 2014). The cores were then embedded in a matrix of compressed expanded graphite and encapsulated in a seamless Ti-Grade 5 cylinder. The figure also shows the profile of power/energy density deposited in the tantalum cores by a single pulse of proton beam, estimated by means of FLUKA Monte Carlo simulations (Ferrari et al., 2005). The relativistic proton beam penetrates over the whole target length, reaching a maximum deposited energy density of 4.5 kJ/cm^3 in the bulk of core no. 4. The duration of such pulse is only 0.9 μs, leading to a maximum deposited power density of 5000 MW/cm^3.

Details about the HRMT-42 target manufacturing, experiment execution and first non-destructive post experiment examinations are reported in Ref. Torregrosa et al. (2018). The most remarkable result arose from a neutron tomography performed after the experiment, which revealed the presence of voids in the bulk of the tantalum cores, with sizes ranging from a few tens of micrometres up to 1 mm. Even more interesting was the fact that the larger voids were not necessarily observed in the cores exposed to higher temperatures and tensile pressures (cores 4, 5 and 6) or, even within the same core rod, in the zones exposed to more extreme conditions such as close to the beam axis. In that study, it was suggested that the origin of these voids may be strongly related to spall fracture which, for ductile metals such as tantalum, is characterized by the nucleation of trans- and intergranular voids and their subsequent growth and coalescence in material exposed to high dynamic loading (Meyers and Aimone, 1983; Llorca et al., 2000a; Antoun et al., 2003; Thissell et al., 2003; Zurek et al., 1996; Czarnota et al., 2006; Molinari et al., 2014).

It is particularly interesting the unique and unprecedented conditions at which this spall fracture has taken place. Historically, there has been two main experimental methods to induce this dynamic process at strain rates above 10^3 s^{-1}; (i) flyer plates (accelerated by explosives or gas guns) and (ii) direct energy deposition by lasers (Remington et al., 2017). All these methods have in common the generation of a very intense stress or shock wave-front, commonly following uni-axial strain, travelling from one side of the specimen in which the front is created, either by mechanical impact or by the sudden expansion of the heated surface material by the laser. This compressive stress front is then reflected as a tensile or a set of rarefaction waves when it reaches the other stress-free surface of the specimen. If the composed amplitude of these tensile waves exceeds the local tensile strength of the material, nucleation, growth and coalescence of voids take place (spall). Subsequent fragmentation can occur if the voids evolve to the degree that the body separates into distinct parts. As presented in the current study, this is not the case of the HRMT-42 target core for several reasons: (i) The load comes from the bulk material, being highly hydrostatic, (ii) the strain state is mostly triaxial, (iii) tensile stresses are due to a mode excitation, that subjects the core to a series of hundreds of compression–tension oscillations, and (iv) these dynamic processes take place at temperatures well above 1000 °C.

The observation of these voids by the neutron tomography led to the target opening, core extraction and subsequent tantalum slicing for metallographic inspection combining optical microscope (OM) and Electron backscatter diffraction (EBSD) measurements (Fornasiere, 2020).

The goal of this study is to describe in detail the observed spalling and the conditions at which has occurred. This is done by linking simulations with the post-test observations. In addition, it will provide different hypotheses aiming at explaining the void distribution revealed. In particular, why these voids appear following a “crown” around the beam axis, and why the largest voids are observed in cores no. 9–10, whereas core no. 4 is more loaded, as shown in Fig. 1.

For this purpose, simulations results for both (i) target progressive heating due to the irradiation time history, as well as the (ii) fast dynamic response after every proton pulse impact are shown in Section 2. The performed dynamic simulations consider the geometry as a continuous, i.e. no voids or cracks are simulated. A more advanced modelling of voids and porosity growth using complex models such as Gurson type (Gurson, 1977) is not within the scope of this work.

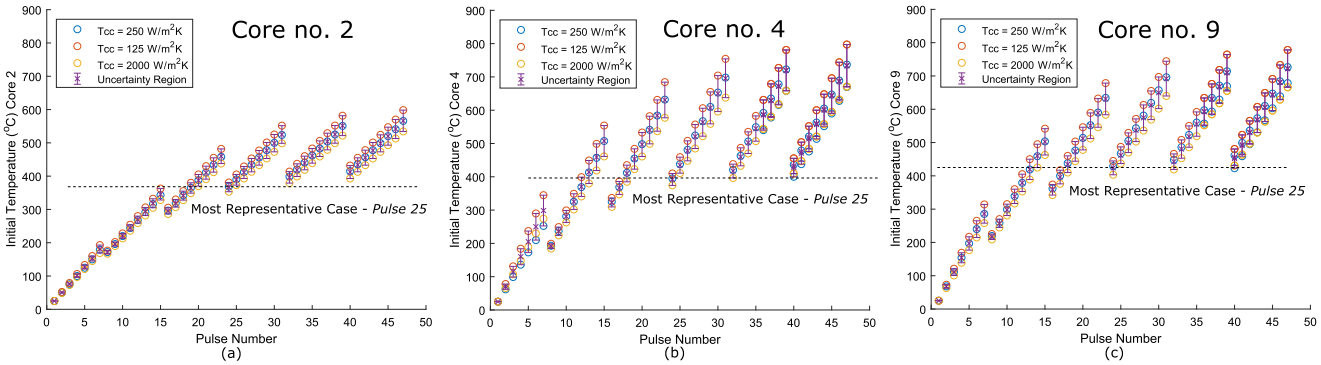

Fig. 2. Estimates of initial temperatures in the cores 2, 4 and 9 right before each of the 47 proton pulse impacts. Three different values of the TCC between the cores and the EG matrix have been selected to assess the uncertainty range.

In Section 3 we present the most relevant observations of the voids and recrystallization in the cores after the experiment. The post-experiment and simulation results are then contrasted in Section 4. Finally, discussion about the governing mechanisms are included in Section 5.

2. Conditions experienced by the tantalum cores

In order to estimate the mechanical and thermal loading experienced by the Ta cores, it is required to analyse phenomena that take place in different time ranges, and thus necessitate different models and computational techniques;

1. Fast deposition of energy by the proton beam, adiabatic temperature rise and dynamic response of the cores: this phenomenon takes place in the order of tens of microseconds. The hydrocode AUTODYN® is employed for this purpose. The thermal and structural solutions are fully coupled. Heat transfer is not taken into account as it is considered negligible in this time frame.
2. Heat diffusion within the target cores after each pulse impact: this process takes place in the order of milliseconds. It will allow estimating for how long the cores were exposed to high temperatures. This is relevant since recrystallization was observed in some of the cores. These calculations are done by means of the thermal solver of ANSYS Mechanical®.
3. Progressive heating due to successive proton beam impacts: up to 47 proton beams were impacted within 6 impacting series. The proton pulse repetition rate was 40 s, with cooling times of 10–15 min between the series. The target was not actively cooled, therefore, a temperature build-up in the cores took place during the experiment. This temperature history, taking place in the order of 2.5 h, is also estimated by means of the thermal solver of ANSYS Mechanical®.

As expected, the progressive heating would definitely affect the initial conditions before every new proton beam impact and therefore, each dynamic response. However, it is not practical to simulate the dynamic response of each of the impacted pulses. Instead, it was considered more suitable to find a range of initial temperatures which could be more representative of the entire experiment, and investigate the dynamic response within this range.

It is worth noting that the simulation results presented in this study shall be considered as estimates, since they are subjected to several assumptions and uncertainties. In order to cope with such uncertainties, several sensitivity analysis have been carried out, aiming at defining the boundary ranges within conditions that led to the observed spalling.

The next three subsections present the simulations in the three time-physics regimes, from the slowest processes to the fastest ones: first, the overall and progressive target heating analysis is presented. Secondly, a thermal analysis of a single pulse considering its heating and cooling

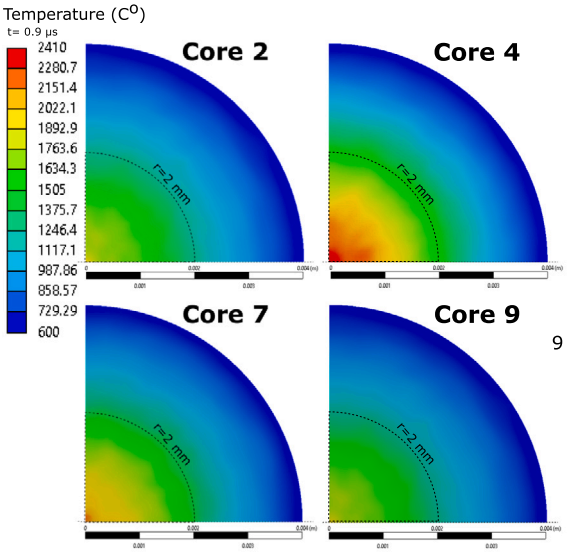

Fig. 3. Estimated temperature profile in the central cross-sections of cores 2, 4, 7 and 9 right after the 25th proton pulse impact, considered as a representative pulse. Higher temperatures were reached in subsequent pulses. Maximum temperatures estimated within 2600–2700 °C were reached in core no. 4 in pulse 47.

stage (selected as the representative one for the whole irradiation). Finally, we present the dynamic response induced in this specific pulse scenario, resolving to the pressure and stresses oscillations that led to the spalling voids.

2.1. Thermal-transient analysis of the target progressive heating

Every proton pulse impacted onto the target deposited around 11.8 kJ of total energy, with a peak energy density of maximum of 4.5 kJ/cm^3 at core no. 4, which lead to an adiabatic rise of temperature in the order of 1800 °C per pulse. Heat diffusion across the target core and matrix makes the temperature peak drop relatively fast, reaching a homogeneous temperature distribution within each core well before the next pulse impact after 40 s.

The goal of the current thermal analysis is to provide a range of initial temperatures present in each core right before each successive proton pulse impact. For this purpose, the whole target geometry (as presented in Fig. 1) has been modelled in ANSYS-Thermal®. The thermal transient simulation considers the power deposited by each of the 47 pulses, following the imposed irradiation sequence. The thermal load of each impacted proton beam is applied as an Internal Heat Generation in the software. The values for such heat are interpolated into the model from results of the deposited energy distribution calculated

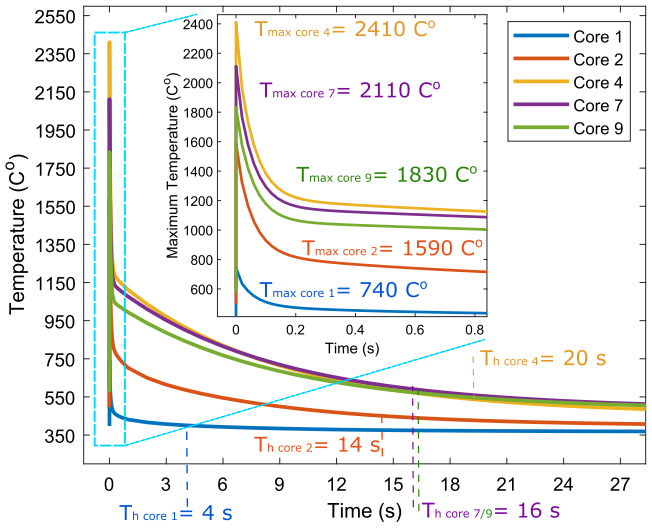

Fig. 4. Estimated maximum temperature history in cores 1, 2, 4, 7 and 9 during 27 s after the 25th proton pulse impact. The time in which a homogeneous temperature is reached within each core is highlighted in the plot as T_h.

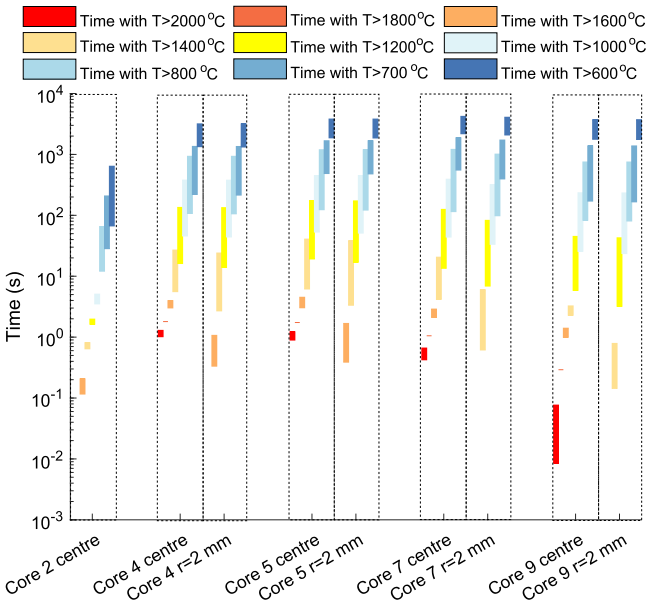

Fig. 5. Time–temperature map that indicates for how long a particular zone of a core has been exposed to a temperature higher than a certain value considering the whole irradiation sequence. The height of the coloured rectangles represent the time uncertainty region, when considering a TCC of 2000 W/m^2 and 150 W/m^2 at the cores-matrix interface.

by means of FLUKA Monte Carlo simulations (Ferrari et al., 2005). Since there was no active cooling of the target, a natural convection coefficient of 5 W/m^2 is assumed in the external surface of the capsule.

The main uncertainty in these estimates comes from the value of the thermal contact conductance (TCC) between the tantalum cores and expanded graphite matrix (EG), which cannot be estimated easily. Mikic correlation has been used for this purpose (Rohsenow et al., 1998) considering different contact pressures between the matrix and the cores. This contact pressure comes from the radial expansion of the EG matrix due to Poisson effect while compressed (in the longitudinal direction) inside the Ti-Grade 5 capsule during the manufacturing (Torregrosa et al., 2018).

Fig. 2 shows, for cores no. 2, 4 and 9, the estimated initial temperatures before each proton beam impact considering three different TCC values in the Ta-EG interface; 125 W/m^2, 250 W/m^2 and 2000 W/m^2 (corresponding to contact pressures of 0.5 kPa, 1 kPa and 5 kPa respectively). Other simulations considering more pessimistic values of TCC (such as 30 W/m^2) showed that this would imply melting in cores no. 4, 5 and 6 which is never observed in the post-experiments observations of Section 3.

The figure shows the range of estimated initial temperatures and the respective progressive heat-up. From this plot, one can infer that a quite representative pulse case of the whole experiment could be the number 25, since there were around 6 impacts starting from such conditions, and its initial temperature is also close to the average initial temperature over the entire experiment. In this pulse, uniform initial temperatures in the order of 370 °C, 400 °C and 425 °C for the cores no. 2, 4, and 9 respectively are present. These initial temperatures are the ones considered in the following studies of the next Section 2.2, and the dynamic analyses in Section 2.3.

2.2. Thermal-transient analysis of the adiabatic temperature rise and heat diffusion within the cores

Each of the proton pulses impacted onto the target cores leads to a non-uniform temperature rise within the cores' cross-sections, with a maximum rise of approximately 1800 °C taking place in core no. 4. This temperature rise is in any case influenced by the initial temperature, i.e. pulse number, due to the temperature dependence of specific heat and density. After this temperature rise, heat diffusion within each core homogenizes the temperature profile in the order of 4–20 s after the pulse impact.

Fig. 3 shows the estimated temperature profile at the end of the pulse impact 25 (0.9 μs duration) in cross-sections placed at the longitudinal centre of cores no. 2, 4, 7 and 9. This analysis considers initial temperatures of 370 °C, 400 °C and 425 °C respectively. A significant gradient of temperature in the radial direction in the order of 1000 °C, 1800 °C, 1600 °C and 1200 °C takes place in each of the cores respectively. It is also remarkable the fact that the temperature rise close to the cores' periphery is also considerable, in the order of 300–400 °C. This is an important reason of the radial mode excitation which exposes the core to oscillating pressures as explained in Section 2.3.

Fig. 4 shows the maximum temperature for each of the rods as a function of time corresponding to pulse 25. In the plot, the characteristic time in which the temperature becomes homogeneous along the entire core is highlighted as T_h. These estimates of heat diffusion and temperature histories within the cores are relevant to explain which conditions led to the recrystallization observed in some of their central zones. Following this reasoning, Fig. 5 presents a time–temperature map of the cores 2, 4, 5, 7 and 9, indicating for how long a particular zone of a core has been exposed to a temperature higher than a certain value considering the whole irradiation sequence. This plot is then used to crosscheck with the EBSD observations in Section 3.2 and infer at which conditions recrystallization took place.

2.3. Dynamic response of the cores

A sudden rise in temperature in the bulk material of any given core should lead to its expansion. However, this is prevented by the neighbouring heated material – which also tries to expand – leading to a subsequent increase in pressure. This is the start of the cores dynamic response, which ends up with the excitation of a dominant radial mode of vibration, subjecting it to an oscillating compressing-to-tensile pressure. The present subsection is dedicated to the simulation and description of this phenomenon, which is the origin of the mechanical load leading to the observed spalling.

The hydrocode AUTODYN® is used for this purpose, following a similar approach as in Ref. Torregrosa et al. (2016). These simulations consider the geometry as a continuous, i.e. no voids or cracks are

simulated. The goal is therefore to estimate the magnitude of pressure, stresses, strain rates and overall load characteristics which led to the appearance of the voids with their respective size and spatial distribution. Local stresses and detailed mechanisms dealing with the void nucleation, coalescence and growth are therefore not taken into account in the simulations.

The computational domain comprises the ten core rods, with a Lagrangian structured mesh of 65 μm in the radial direction by 484 μm in the longitudinal one. The thermo-mechanical solution is fully coupled. The only load applied to the geometry is the increase of internal energy due to the proton beam impact during its 0.9 μs duration. The space distribution of such internal energy has been previously calculated by FLUKA Monte Carlo simulations (Ferrari et al., 2005) and, similarly as in the previous thermal analysis of Section 2.1, it is interpolated and applied into the AUTODYN® mesh. The AUTODYN® user function `EXSIE3` is used for this purpose. No external boundary conditions have been applied to the cores, leaving them completely free to vibrate. The possible effect of the surrounding material (such as the EG matrix) in the dynamic response was assessed by simulations in Ref. Solieri (2017), finding a very limited influence on the excitation of the dominant mode.

The tantalum material is modelled through an Equation of State (EOS) and a Strength Model. A linear EOS of the type Mie–Grüneisen has been used (with the formulation available in AUTODYN®). This formulation is given in Eqs. (1) and (2) for compression ($\mu > 0$) and tension $\mu < 0$ respectively (Steinberg, 1996). In the equations, μ is the compression ratio, e is the specific energy, C_0 in the bulk speed of sound, S1 is the 1st order parameter of the shock and particle velocity relation, γ_0 is the Grüneisen parameter and ρ_0 is the initial density.

$$P(\mu, e) = \frac{\rho_0 C_0^2 \mu \left[1 + \left(1 - \frac{\gamma_0}{2}\right)\mu\right]}{\left[1 - (S_1 - 1)\,\mu\right]^2} + \gamma_0 \rho_0 e \tag{1}$$

$$P(\mu, e) = \rho_0 C_0^2 \mu + \gamma_0 \rho_0 e \tag{2}$$

For the Strength Model, two types of formulations have been used, Johnson–Cook (J-C) (Johnson and Cook, 1983) and Zerilli–Armstrong (Z-A) (Zerilli and Armstrong, 1987), as part of a results sensitivity analysis. These models use Von Mises as yield criterion and compute the flow stress taking into account its temperature and strain rate dependence.

The Table 1 summarizes all the models used in the hydrocode simulations, with its corresponding parameters and references.

One of the main uncertainties in the accuracy of the performed simulations comes from the fact that the employed strength models are extrapolated to higher temperatures and strain rates than the ones reached in the dynamic experiments from which the parameters of these models were extracted. In addition, the tantalum material used in the dynamic testing of Ref. Zurek and Gray III (1996) was in annealed conditions, while the one of our cores was non-annealed. In order to evaluate the possible influence of such uncertainty in the results, a sensitivity analysis has been performed.

2.3.1. Sensitivity analysis of the strength model

Simulations using five different strength models have been carried out. Four of them are the ones specified in Table 1 and consider flow stress as a function of temperature and strain rate, whereas the fifth one consists only of the shear modulus, thus it considers that the material behaves infinitely elastically and plastic yield is never reached.

The parameters for the temperature and strain rate dependent Johnson–Cook and Zerilli–Armstrong models belonging to the Ref. Zurek and Gray III (1996) were obtained from data fit of Hopkinson Bar tests (Hopkinson, 1914) only in compression, carried out in the temperature range from 25 °C to 1000 °C and strain rates from 10^{-1} s^{-1} to 3900 s^{-1}. These models provided good agreement within 15%–20%

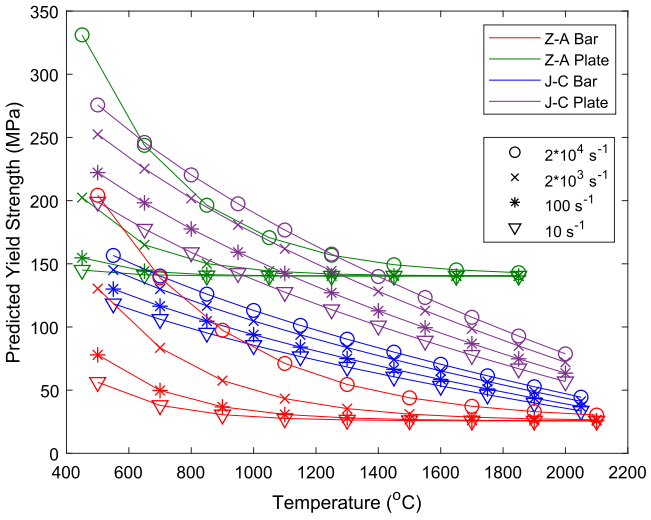

Fig. 6. Comparison between the yield strength predictions by the four strength models considered for the strain rates and temperature ranges present in the cores.

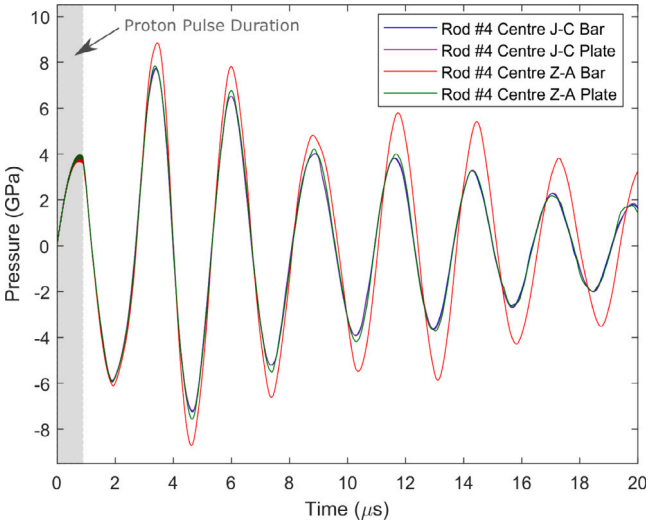

Fig. 7. Comparison between the simulated pressure response at the centre of core no. 4 (the most loaded one) considering the four different strength models introduced in Table 1.

of strain of the experimental strain–stress curves. On the contrary, in the tantalum cores of our experiment, the material is subjected to both tension and compression, maximum temperatures reach 2600–2700 °C, and estimated strain rates reach up to $3 \cdot 10^4$-$4 \cdot 10^4$ s^{-1}. As a consequence of the extrapolation, these models predict a broad variety of different values of yield strength within this range of conditions, which are summarized in Fig. 6. It can be seen for instance that at 500 °C and $2 \cdot 10^4$ s^{-1} the yield strength predicted by the model Z-A Plate model are 310 MPa while for Z-A bar is 200 MPa. At this temperature and lower strain rates (10^1 s^{-1}), the range of prediction becomes even broader; from 50 MPa to 200 MPa predicted by the Z-A bar and J-C bar models respectively. At high temperatures, the strain dependence vanishes for all the models (something observed also in the experimental data of Ref. Zurek and Gray III (1996) up to the maximum temperature tested of 1000 °C). Nevertheless, the different models still predict a wide range of yield strength at 2000 °C; from 30 MPa for Z-A bar up to 140 MPa for Z-A plate.

Fig. 7 shows the predicted pressure response during 20 μs after the pulse impact in the centre of core no. 4 considering the four different

Table 1
Different material parameters used in the hydrocode simulations. Z-A stands for Zerilli–Armstrong model Zerilli and Armstrong (1987), J-C for Johnson–Cook model Johnson and Cook (1983). Bar or Plate stands for the form of the raw material dynamically tested (which was forged). The tested tantalum material was in annealed conditions Zurek and Gray III (1996). The strength model selected for the simulations of Section 2.3.2 is the Z-A bar.

Equation of State (EOS)								
Type		ρ g/cm^3		γ	S_1	C_0 m/s		Comments
Mie–Grüneisen		16.69 (at RT)		1.67	1.2	$3.41 \cdot 10^3$		Used in all the analysis. From Ref. Steinberg (1996)
Strength model								
Type	Shear modulus GPa	C_0 MPa	C_1 MPa	C_3 $\cdot 10^{-3}$ K^{-1}	C_4 $\cdot 10^{-4}$ K^{-1}	C_5 MPa	n	Comments
Z-A Bar	65.6	25	1040	5.525	3	480	0.575	Selected Model. From Ref. Zurek and Gray III (1996)
Z-A Plate	65.6	140	1750	9.75	6.75	650	0.65	From Ref. Zurek and Gray III (1996)
Type		A MPa	B MPa	n	C	m	T_{melt} K	Comments
J-C Bar	65.6	185	675	0.3	0.047	0.425	3250	From Ref. Chen et al. (1996)
J-C Plate	65.6	340	750	0.7	0.0575	0.4	3250	From Ref. Zurek and Gray III (1996)

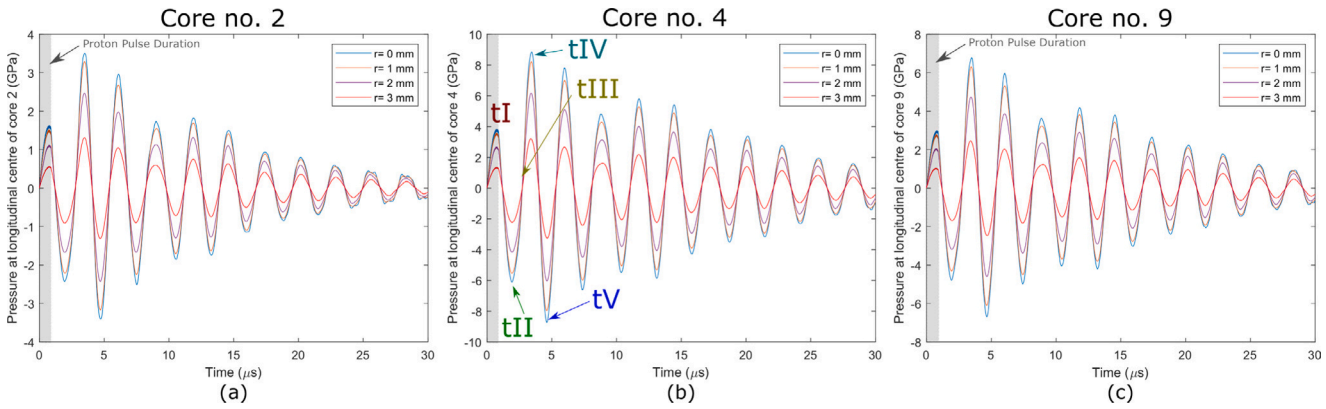

Fig. 8. Dynamic response of the pressures during 30 μs after the beginning of pulse impact at the longitudinal centre of the cores 2, 4 and 9 respectively and for the radial positions at 0 mm, 1 mm, 2 mm and 3 mm.

strength models discussed. As it can be seen in the figure, the great difference in yield strength predictions has a limited effect on the pressure response, leading to only a 18% variation of the maximum reached tensile pressure (taking place at around 4.6 μs after the pulse). This limited influence is attributed to the high triaxiality factor of the load (shown in detail in Fig. 10 of Section 2.3.2) that induces that the response is mainly dominated by the hydrostatic component of the stress tensor, which is governed by the EOS rather than the strength model.

The main difference in the predictions of Fig. 7 resides in the damping time on the radial mode, which takes place due to the plastic work that is accumulated during each oscillation. The Z-A bar strength model gives slower damping since the predicted plastic work is lower. This is explained by the lower yield strength and higher softening at high temperatures predicted by this model in comparison with the others as shown in Fig. 6.

Based on this sensitivity analysis, it can be concluded that a 15%–20% uncertainty in the maximum tensile pressure predicted by the hydrocode simulations is present due to the strength model extrapolations. Nevertheless, the simulation results presented from now on correspond to the ones using the Z-A bar strength model. This selection is done based on the higher softening prediction at the highest temperatures (30 MPa at 2000 °C) which is more consistent with the 11 MPa of tantalum yield strength at 2000 °C and quasi-static conditions reported in the literature (Browning et al., 2017).

2.3.2. Characteristics of the dynamic load in the cores

Figs. 8-(a–c) shows the pressure response during 30 μs after the pulse impact at the longitudinal centre of the cores no. 2, 4 and 9 respectively and for the radial positions at 0 mm, 1 mm, 2 mm and 3 mm. The initial temperatures before the proton pulse impact considered for these cores are 370 °C, 400 °C and 425 °C respectively, consistently with what was estimated in Section 2.1 as the most representative pulse within the 47 impacted. The plots show the response at the longitudinal centre of the cores since it is in this cross-section where the highest compression and tension pressures are reached.

These three plots show the oscillatory compressive-to-tensile nature of the dynamic response, with a period of 2.77 μs, reaching maximum compression and tension pressures of several gigapascals at r = 0 mm. In addition, it is important to note that the pressure response at different radial locations is in phase, indicating that the response is consequence of the excitation of a mode of vibration that comprises the whole core geometry. This mode is excited in such a way for two main reasons; (i) The proton pulse length (0.9 μs) is between 1/4 and 1/2 of the natural period of the mode. (ii) The proton pulse impact suddenly heats-up and induces expansion of the entire cross-section of the cores (as shown in Fig. 3). More details of the peculiarities of this mode

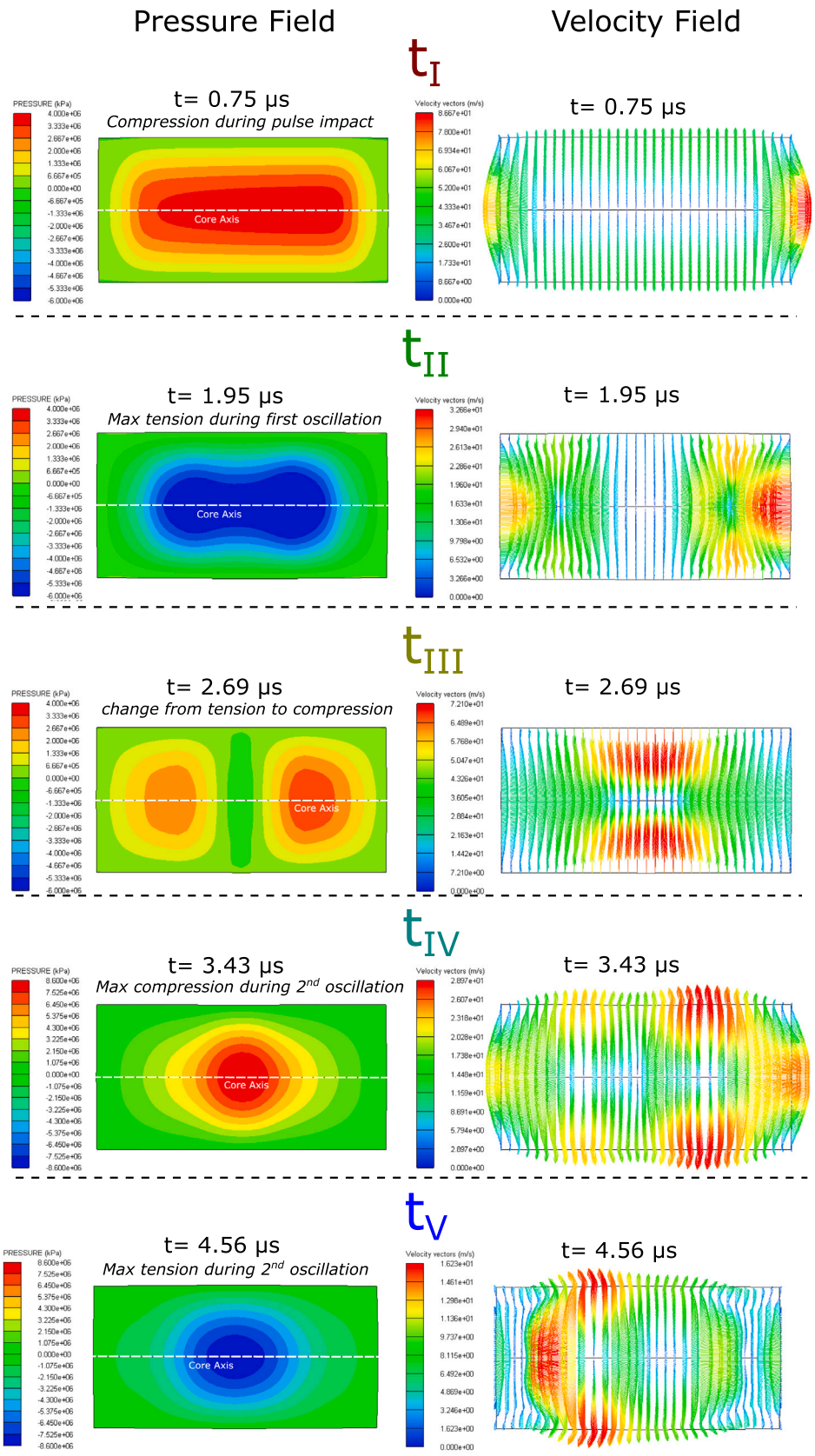

Fig. 9. Contour plots of pressure field (left) and velocity field (right) at the longitudinal cross-section of core no. 4 at five relevant times corresponding to the labels tI, tII, tIII, tIV and tV marked in Fig. 8. In the pressure plots, red represents compression, blue represents tension and green represents areas with low pressure loading (below 700 MPa in t_I, t_{II} and t_{III}, below 2 GPa in t_{IV} and t_V). (For interpretation of the references to colour in this figure legend, the reader is referred to the web version of this article.)

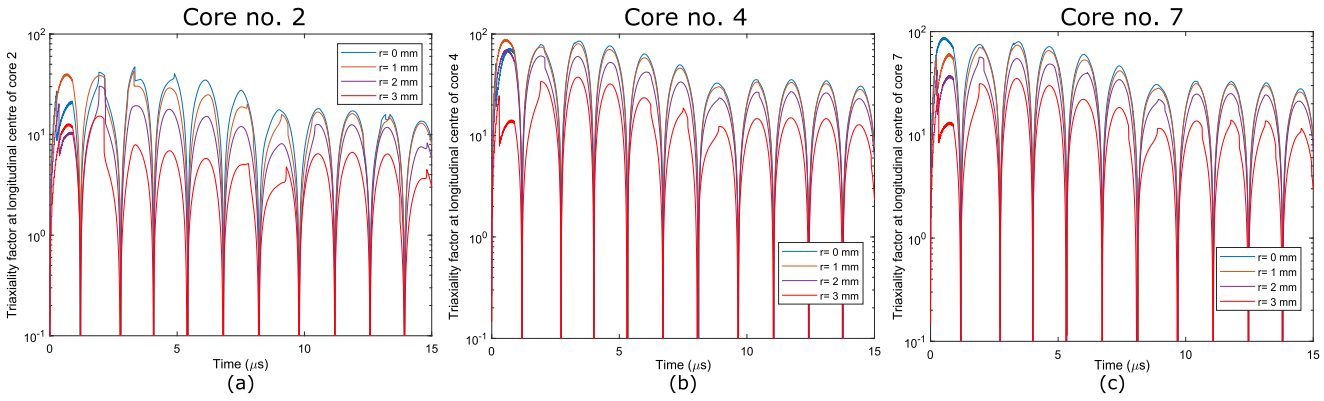

Fig. 10. Triaxiality factor (defined as absolute Pressure/flow stress) at different radial positions of the longitudinal centres of the cores 2, 4, and 7 respectively.

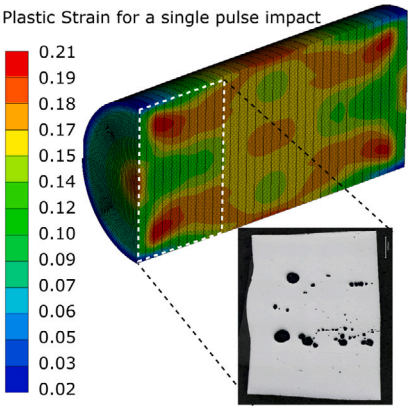

Fig. 11. Contour plot of the estimated plastic strain distribution within half-cut of the core no. 4 for a single proton pulse impact. The shape of the predicted deformation is consistent the one of the cores after the experiment.

excitation, numerical and analytical, can be found in Refs. Torregrosa et al. (2016) and Solieri (2017), Torregrosa (2018) respectively, as well as experimental measurements in Ref. Torregrosa et al. (2019b).

The contour plots of pressure and velocity fields in a longitudinal cross-section of the core no. 4 are presented in Fig. 9 to better illustrate the characteristics of the dynamic response and its space distribution. These contour plots are presented for five representative times, marked as tI, tII, tIII, tIV and tV in Fig. 8:

1. tI corresponds to t = 0.75 μs after the beginning of the pulse impact (while it is still depositing energy). At this time, the highest compressive pressures of the first oscillation are reached (4 GPa), consequence of the temperature build-up. The velocity field shows the fast expansion of the core peripheries with velocities in the order of 50–80 m/s. These velocities will continue growing due to inertia, until t ∼ 1.3 μs (1/2 of the mode period) when the cohesive forces of the material start pulling it back, with the subsequent velocity reduction.
2. tII corresponds to t = 1.95 μs, when the maximum tensile pressure of the first oscillation is reached in the bulk. At this moment, the velocity at the radial periphery of the core is almost 0, and corresponds to the shift from expansion to compression.
3. tIII corresponds to t = 2.69 μs, when the pressure in the longitudinal centre of the core is close to 0. At this time, the velocities at the core radial periphery towards the centre of the rod are maximum (72 m/s).
4. tIV corresponds to t = 3.43 μs, when the highest compressive pressure over the dynamic response is reached, close to 9 GPa. This takes place in the second mode oscillation and it is consequence of the merging of two compressive fronts travelling from the core sides (showed in the previous plot at t = 2.69 μs).
5. tV corresponds to 4.56 μs when the highest tensile pressure over the response is reached, estimated in 8.7 GPa, taking place in the second mode oscillation.

As shown in Fig. 8, the pressure oscillations illustrated by the contour plots continue until their damp by the dissipation of energy in plastic work. As a matter of fact, it is important to remark that the tantalum material experiences plastic deformation in every compression and tension oscillation. According to the simulations, a damping down to the 1% of the maximum pressure reached in the first oscillation takes place in the order of 15 oscillations. Nevertheless, this damping may be over-estimated by the simulations in view of experimental measurements observed in Ref. Torregrosa et al. (2019b). In any case, it can be claimed that, taking into account the 47 impacted proton pulses, the tantalum cores were exposed to at least 700 compressive-to-tensile oscillations over the experiment, leading to the spall formation.

An important characteristic of the dynamic response is its highly triaxial nature. This triaxiality as a function of time is illustrated in Fig. 10 at different radial positions of the longitudinal centres of the cores no. 4, 7, and 9 respectively. In such plots the triaxiality is defined as the absolute value of pressure divided by the flow stress. As shown in the plots, the triaxiality is above 10 for most of the time even in the less loaded cores (such as core no. 2), and not only in the centre but in regions closer to the cores periphery (r = 3 mm). The highest triaxiality factor is reached in the centre of core no. 4 (up to 90), being above 50 even at r = 3 mm. This load characteristic is attributed to the triaxial nature of the sudden thermal expansion and the material softening associated to the high temperatures reached, which prevent the rise of deviatoric stresses.

Another aspect that can be observed in Figs. 8 and 9 is that high tensile pressures above 2 GPa are reached, not only in the centre of the cores, but at r = 3 mm (75% of the radius). The maximum tensile pressure is different in each core depending on the different temperature rise (Fig. 4). This is consistent with the longitudinal profile of energy deposited by the beam (Fig. 1). The maximum tensile pressures estimated for each core is 0.75, 3.5, 7.1, 8.7, 8.8, 8.3, 7.7, 7.2, 6.64, 6.1 GPa for cores 1–10 respectively.

Finally, Fig. 11 shows a contour plot of the estimated plastic strain within core no. 4 after 80 μs (when the response is damped) considering a single pulse impact. As it can be seen in the figure, the maximum plastic strains per pulse are in the order of 20%. This strain is clearly non-uniaxial, differently from other conventional setups reaching such high dynamic loads. The simulated plastic strain distribution is also consistent with the deformed shape of the cores observed (also shown in the figure), presenting protuberances at the sides of the core axes.

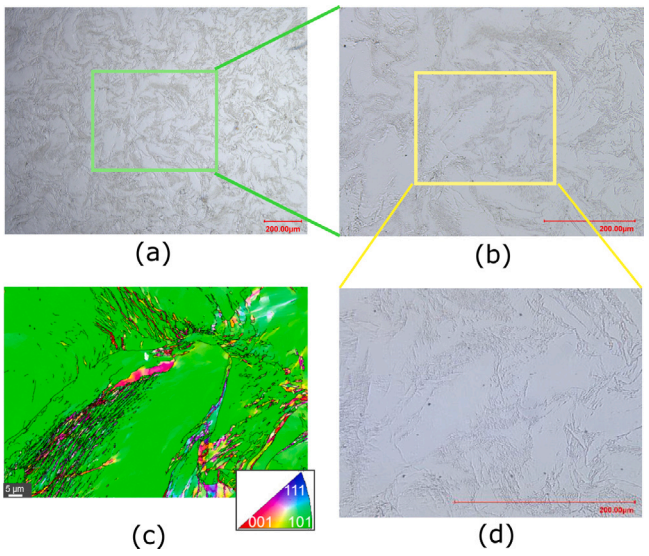

Fig. 12. OM images of the central regions of a Ta rod in pristine conditions, obtained from the same batch as the tested material. Images and the EBSD show a highly deformed microstructure with no clearly defined regular grains. All black lines in (c) are grain boundaries (10° or 15° change in crystal orientation).

3. Post-experiment examinations of the Ta cores

After one year of radioactive decay to minimize exposure to personnel, the target was opened and the Ta rods were retrieved from the expanded graphite matrix. Then, a slice of 4 mm thickness was cut from the longitudinal centre each of the rods. The extremities of such slices were polished and prepared for metallographic inspection combining optical microscope (OM) and Electron backscatter diffraction (EBSD) measurements. Therefore, two transverse samples per core have been analysed. These transverse cuts correspond to the slices at ±1.5 mm with respect to the longitudinal centre of the cores (taking into account the removed material during polishing). In addition, partial longitudinal cuts were also analysed for the cores no. 7 and 8. The cross and longitudinal sections were then mounted in phenolic resin, mechanically ground (with P600, P1200 and P2400 grit paper), polished with diamond suspension (3 μm and polished with colloidal silica suspension. Chemical etching was carried out between each step by immersing the sample for 90 s in solution no. 66 from standard ASTM E407 (AST, 2015). OM pictures were acquired with a digital microscope KEYENCE VHX 1000.

3.1. OM images of the voids

Fig. 12 shows reference images of the pristine Ta material, obtained from transversal cuts of the 8 mm diameter rods received from the supplier PLANSEE (Obererlacher, 2014). Such rods were forged and delivered in non-annealed conditions. The highly deformed microstructure consequence of the manufacturing process is clearly observable in the optical image with x1000 magnification of Fig. 12-(d), in which no clearly defined regular grains and grain boundaries are present (confirmed by the EBSD image of Fig. 12-(c)). In addition, these images reveals the absence of observable voids or second phases in the pristine material within the achieved resolution. Therefore, it cannot be inferred that the spalling voids nucleated from existing second phase particles or micro pores.

As already introduced and observed in the neutron tomography of Ref. Torregrosa et al. (2018), a large number of voids have formed, presenting a wide range in size distribution, from 2 μm up to 750 μm equivalent diameter. The pictures of Fig. 13 illustrate the non-uniform space distribution of such voids, present both when comparing different cores as well as when comparing radial zones within the same core. For instance, cores no. 2, 8 and 9 clearly present larger voids, above 100 μm distributed homogeneously within the radial zones with $0 < r < 2$ mm. On the other hand, for cores no. 3, 4, 5 and 6 voids are considerably smaller, scarce and isolated in the centre while larger in the radial zone 1 mm $< r <$ 2 mm, following a "crown-like" distribution. No voids were found the slice 1 of core no. 2. This could be attributed to the significant longitudinal gradient in temperature present in this rod, which makes that tensile pressures in the first slice were below the onset for spalling, or just by the coincidence that the cut was performed in a section between voids.

Fig. 13 shows microscope observations of all the transverse cuts along the central cross-sections from core no. 2 to core no. 9, in which the spalling voids can be clearly observed. In addition, these figures include a longitudinal contour plot with the estimated temperature reached in the pulse 25. In this way the difference magnitude of temperatures (and pressures) reached within rods can be assessed.

The non-uniform size and space distribution of the voids illustrated in the pictures of Fig. 13 indicates differences in the process of void growth and coalescence depending on the region and core, i.e, the loading conditions. A detailed analysis of voids size and density distribution obtained by computer image analysis is included in Fig. 19 of Section 4 in order to link between these different trends and the respective conditions.

Fig. 14 shows images of the cuts performed along the longitudinal direction of the cores no. 7 and 8. These images show that voids are present from a distance as close as 1.5 mm from the longitudinal extremity of the rod. The "crown-like" void distribution is particularly remarkable in core no. 7, with visible lines of void concentrations along the 1 mm radius. The shape of the voids appears relatively regular and spherical when they are small enough. Nevertheless, several large voids with an oval preference in the longitudinal direction can be observed in the longitudinal cut 2 of core no. 7 and both longitudinal cuts of core no. 8. The axisymmetric nature of the load and low gradient along the longitudinal direction imply that the thermal and pressure conditions along a specific radial region are relatively constant. Therefore, if in certain conditions the void growth is enhanced, this oval preference could be consequence of an increased coalescence along the longitudinal direction in certain radial regions (such as along the 1 mm radius) in which the void concentration is higher.

3.2. Presence of recrystallization and comparison with pristine material

High precision EBSD mappings were acquired with SEM (ZEISS) on specific parts of the sliced cores in order to characterize and identify changes in the microstructure as a consequence of the loading. Mappings were acquired employing an accelerating voltage of 20 kV, aperture diameter of 1.2 μm and a working distance of 16 mm. For the grain orientation mappings, grain boundary threshold was fixed at 10° and the inverse pole figure respect to the z-direction. These analyses are summarized in Figs. 15–18, in which EBSD results within three regions of the slices of cores no. 4 and 9 are presented. These regions correspond respectively to the centre of the rods, a radial region within 1–1.5 mm, and within the periphery. The comparison between core no. 4 and 9 is selected based on the significant difference in the voids size distribution between these two; many small voids in the former while a few very large voids in the latter.

The EBSD maps for the central region of rod no. 4 (Figs. 15 and 16) show a complete recrystallization at these locations with significant grain coarsening. The final grains are equiaxed with grain sizes varying from 5–10 μm for the smallest grains, up to 50–100 μm for biggest. This recrystallization and coarsening is definitely consequence of the loading, since such clear grain definition was not present in the pristine material shown in Fig. 12. In addition, the initial highly distorted

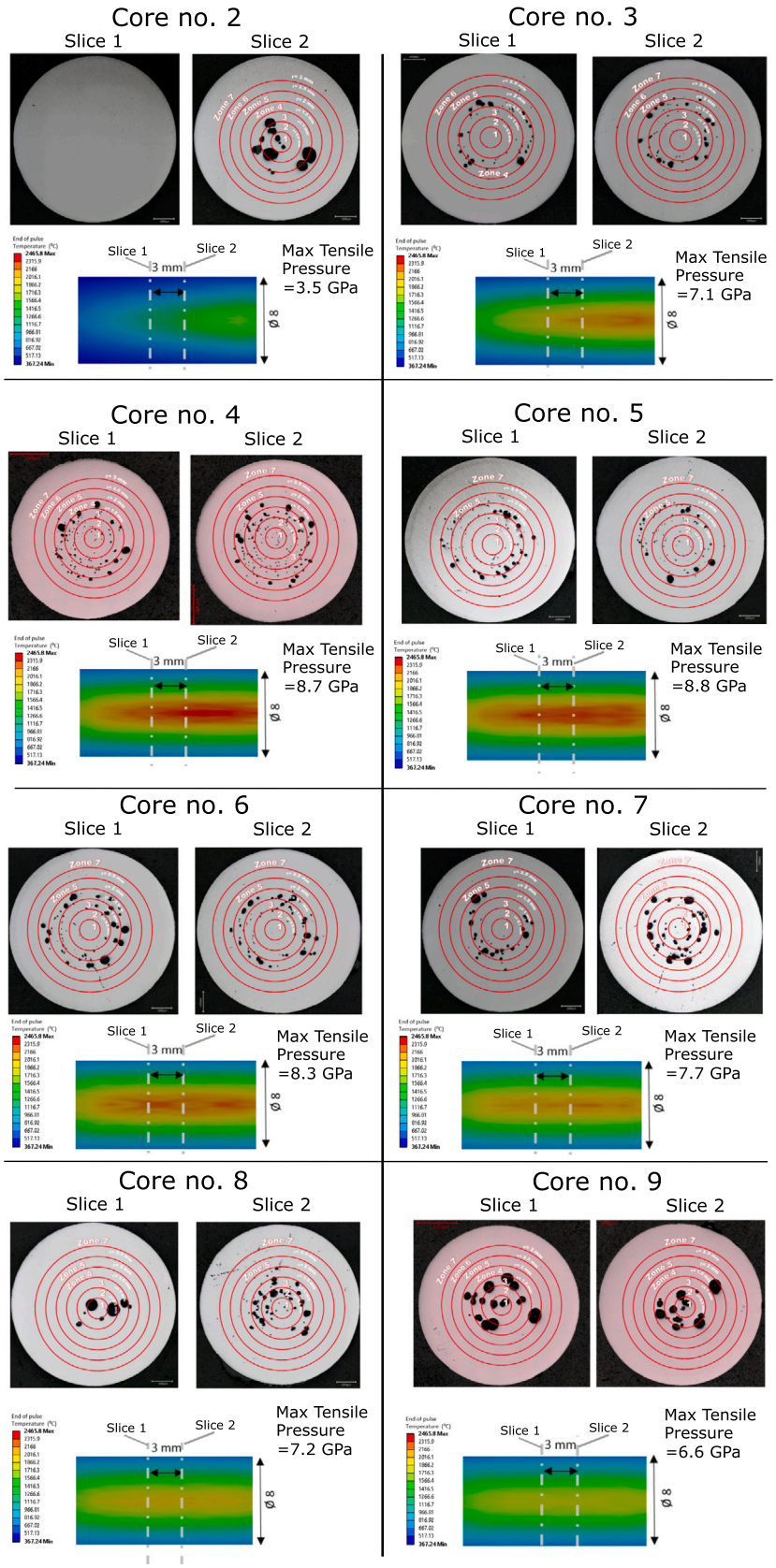

Fig. 13. OM images after slicing and polishing the cores no. 2–9. Below, a contour plot with the reached temperature at pulse 25 with the indication of the position of the slices. Maximum tensile pressure estimated in each core is also indicated.

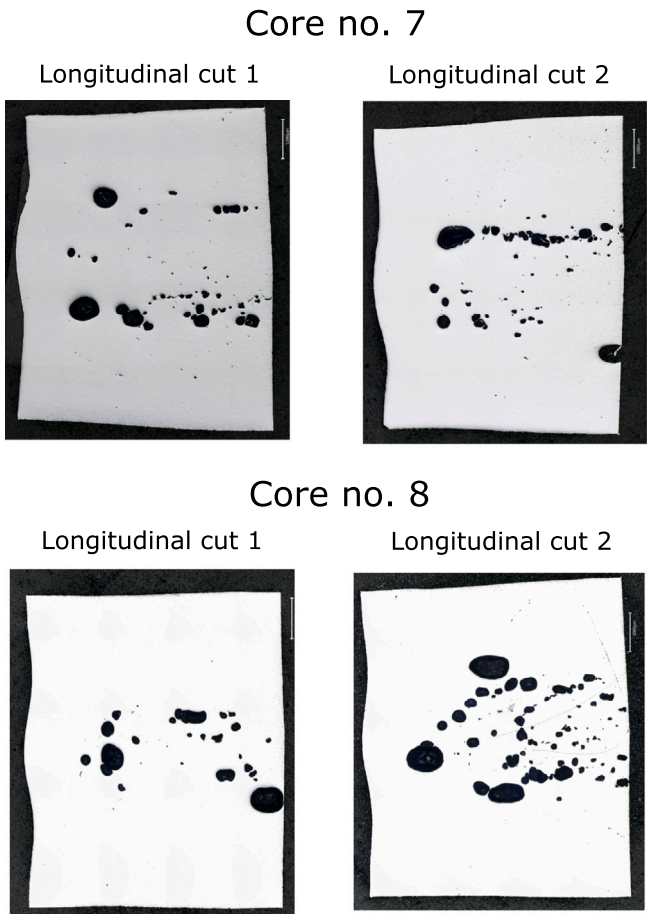

Fig. 14. OM pictures of longitudinal cuts performed on the extremities of cores no. 7 and 8. Some of the larger voids present an oval shape with preference in the longitudinal direction probably due to higher presence of voids and their coalescence in specific radial regions.

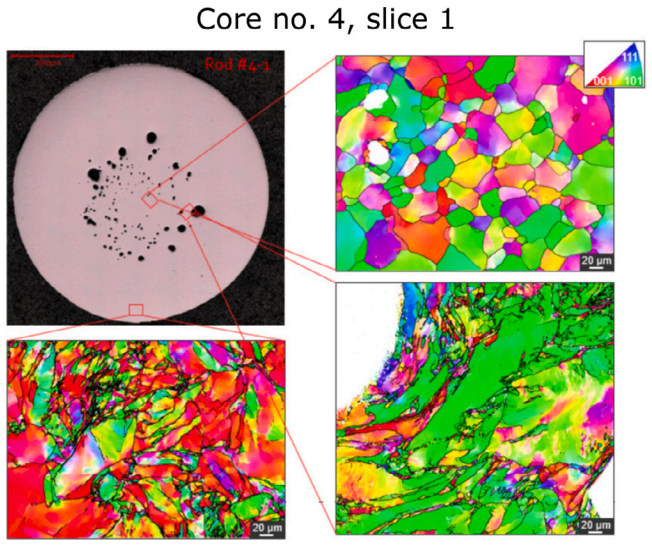

Fig. 15. OM and EBSD images of slice 1 in core no. 4. This core belongs to the most loaded ones in terms of temperature and tensile pressures. It presents a large amount of small voids following a "crown-like" distribution. EBSD images indicate that thermally induced recrystallization has taken place in the central regions.

microstructure is fully present the periphery as well as mostly present in the radial region of 1.5–2 mm.

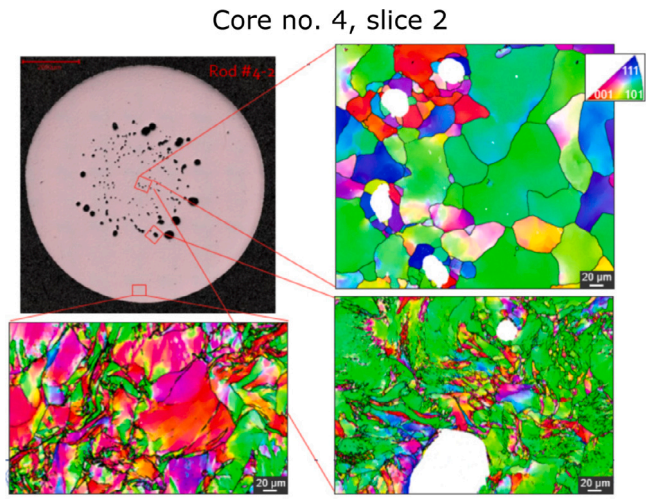

Fig. 16. OM and EBSD images of slice 2 in core no. 4. Similar features as the ones in slice 1 of core no. 4 of Fig. 15.

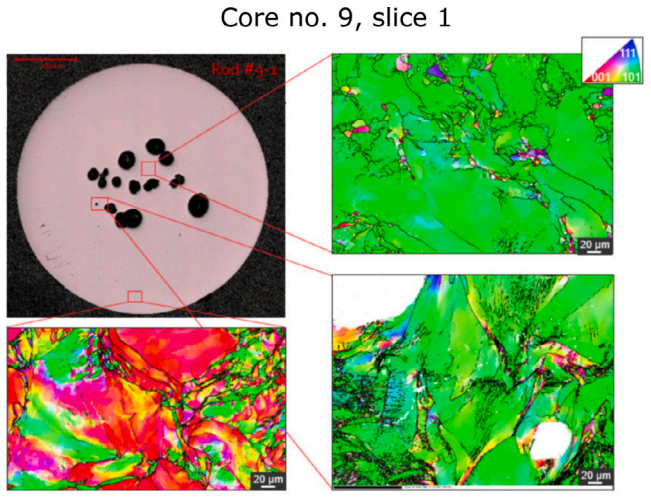

Fig. 17. OM and EBSD images of slice 1 in core no. 9. A few large voids are present in this core. EBSD images indicate absence of recrystallization, differently from the central regions in core no. 4.

This new grain formation in the central regions of core no. 4 (implying nucleation and growth) seems to be thermally induced considering the high temperatures reached there (above 2000 °C, being present during up to 2 s) according to the estimates of Fig. 5, which was taking into account the 49 impacted pulses. In addition, this figure also shows that these central regions were above 1600 °C for nearly 3–4 s. These times and temperatures for recrystallization in Ta seem to be compatible with what has been reported in literature, in particular in Ref. Kerisit et al. (2013), in which in-situ EBSD measurements suggest that incipient recrystallization can take place after annealing at 1030 °C for just 2 s, with subsequent grain growth rate at about 1.5 μm/s when exposed to 700 °C for several seconds. Temperatures in our case were significantly higher, although the exposure times were shorter.

It is remarkable in any case that the fully developed recrystallization did not take place at the radial region of 2 mm of core no. 4, nor in any region of core no. 9 (shown in Figs. 16 and 17), in which temperatures and times were relatively lower. It is true in any case that at 2 mm of core no. 4 and at the centre of core 9. there are already a few new grains appearing at the old grain boundaries, so recrystallization was somehow already triggered there. Relating the

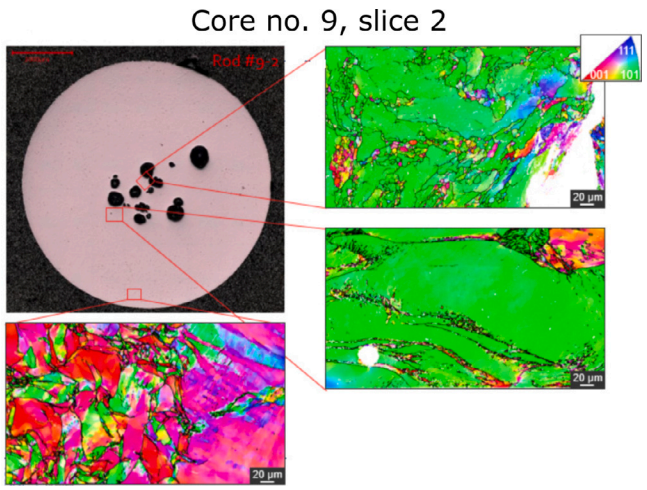

Fig. 18. OM and EBSD images of slice 2 in core no. 9. Similar features as the ones in slice 1 of core no. 9 of Fig. 18.

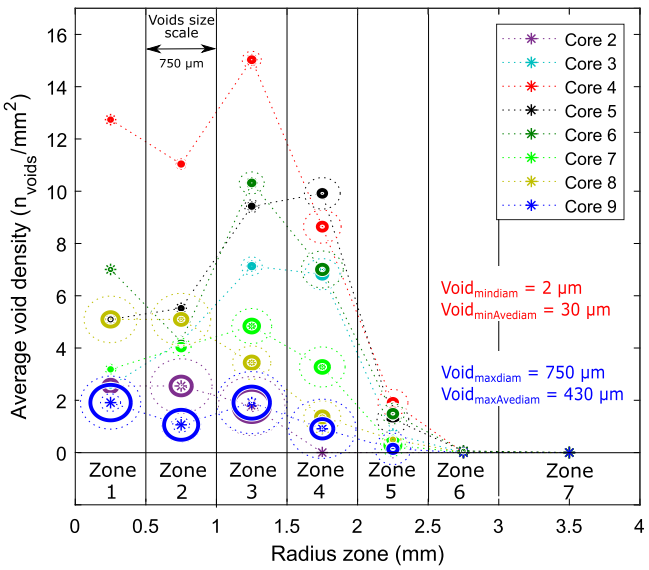

Fig. 19. Plot showing a quantitative analysis of average voids density and sizes within seven discretized radial zones (highlighted in Fig. 13) for cores 2–9. The plot is obtained from the analysis of 16 transverse cuts (2 per core) performed within ±2.5 mm from the longitudinal centre of the cores.

EBSD images with the time–temperature map of Fig. 5, one could infer that full recrystallization occurs when exposing the Ta above 2000 °C for nearly 1 s and above 1600 °C for 3–4 s (as happens in the centre of core no. 4). Whereas it is just slightly triggered when exposed to 1600 °C for ~ 1 s and reaching 2000 °C for 0.05 s as in the centre of core no. 9 (suggested by Figs. 17 and 18).

Defining clear boundaries of times and temperatures for characterizing recrystallization grain growth rate from our experiment seems complex if not impossible due to the huge variation of temperatures and exposure times between zones during the irradiation. Nevertheless, it is interesting the confirmation that these recrystallization processes can take place relatively fast as they can be induced by intermittent thermal loads above 1000 °C of just 1 s of discrete duration.

Finally, another remarkable aspect of the EBSD analysis in the recrystallized regions of Figs. 15 and 16 (where void sizes are in the order of 20 μm) is that voids seem to be present in between several smaller grains, rather than surrounded or in the middle of a large grain. This could be in any case consequence of the fact that recrystallization occurred after several pulse impacts, when the incipient voids were already present, so grains grew around the void.

4. Quantitative analysis of spalling void distribution and links with simulations

In order to relate the observed void growth trends and the respective conditions, Fig. 19 provides a quantitative analysis of void density and size distribution for several radial zones within the cores 2–9. To obtain this plot, the 16 cross-sectional cuts of Fig. 13 have been analysed (2 slices per core). The images were computationally post-processed by a script that extracted the equivalent diameter and radial position of each void. This information was then discretized within the 7 different radial zones shown in the pictures (using a radial step of 0.5 mm). In Fig. 19, the average void density (number of voids per square millimetre) within these radial zones is plotted, together with circles that are scaled to represent the average void diameter in the respective zone. Additionally, circles representing the minimum and maximum voids diameter of each zone are also plotted in dashed line. The quantitative analysis of Fig. 19 confirms what is visually suggested from the pictures of Fig. 13. Indeed, in some regions there is a high number of small voids per area whereas in other there is a low number of large voids. This suggests that in the latter many small voids grew faster and eventually merged to create larger voids. Following this approach, three voids tendency regions are identified in the plot:

1. Region with no voids: this corresponds to the zones 6 and 7 ($r > 2.5$ mm) for all the cores. Even if some of these areas were still subjected to tensile pressures of 2–3 GPa, (see pressure response for core no. 4 at r = 3 mm in Fig. 8-(b)) no voids have been formed.
2. Region with a high number of small voids: this could correspond to areas with average void density above 6 voids/mm^2 and associated average void sizes in the order of 70 μm or lower. The most representative of this region could be the areas of $r < 1.5$ mm (zones 1–3) for core no. 4. The areas within $r < 1$ mm (zones 1–2) for cores 5 and 6 could fit as well within this trend, specially from the point of view of small average size. The zone 3 (corresponding to 1 mm$< r < 1.5$ mm) for cores 4–6 could be as well representative due to the high void density and small dimensions.
3. Region with a low number of large voids: this corresponds to areas of $r < 2$ mm of cores no. 2 and 9, where there are around 1–3 voids/mm^2 with average diameters of 250–400 μm, and some of them even reaching 750 μm. The zone 4 (1.5 mm$< r < 2$ mm) for cores 3–6 could be as well – to a lesser extent due to lower density and larger sizes – representative of this region, since some voids with diameters up to 350 μm are present there. As it turns out, the presence of these larger voids in zone 4 for cores no. 3–6 is what visually suggests the "crown" distribution in the image of Fig. 13.

Fig. 20 shows a similar analysis as the one of Fig. 19 but in terms of average porosity within the discretized radial zones of the cores. This plot does not include direct information about the number of voids density and the individual void sizes, but clearly illustrates in which regions there is an effective increase of porosity. The highest averaged porosity is reached in the areas with $r < 1.5$ mm (zones 1–3) for core no. 9, as well as areas within 0.5 mm $< r < 1.5$ mm for core no. 2, with ratios within 0.12 and 0.33. Similarly with core no. 8, in which porosity decreases from 0.175 to 0.1 from the centre to r = 1.5 mm, and then drops down to 0.01 for $r > 1.5$ mm. On the other hand, average porosity is limited well below 0.05 for such central regions in cores no. 3–7, reaching a peak of 0.1–0.14 only in zone 4 (1.5 mm $< r < 2$ mm), representing the "crown-like" distribution observed in such cores.

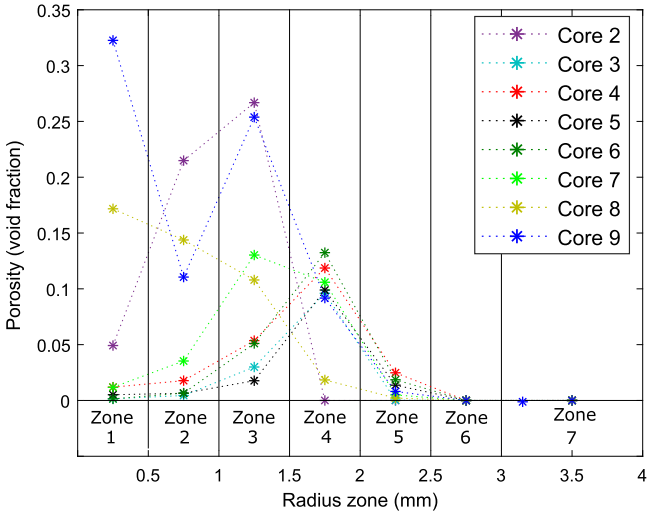

Fig. 20. Plot showing the average porosity (considering two slides per core) within the seven discretized radial zones indicated in Fig. 13.

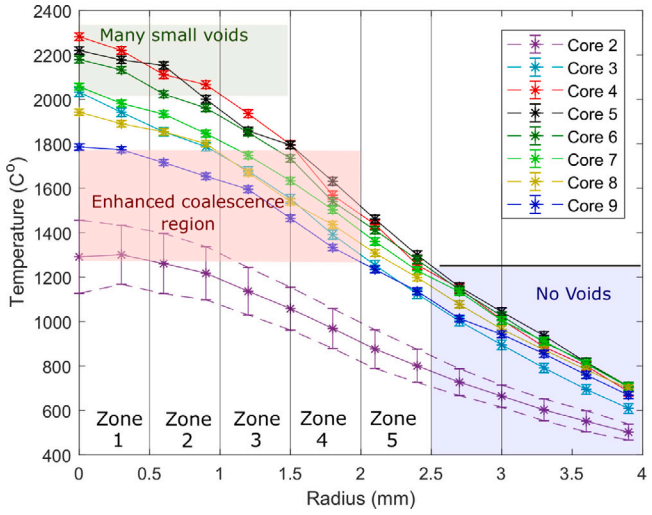

Fig. 21. Estimated radial temperature profile close to the longitudinal centre of cores 2–9 for pulse 25. These temperatures correspond to the ones at which the dynamic response took place. The error bars represent the temperature variation within the cross-sections situated at ±2.5 mm with respect the longitudinally centred one.

The intriguing fact of the non-uniform distribution described is that in the most loaded zones (in terms of temperature and tensile pressures) such as r < 1.5 mm for cores no. 4, 5 and 6, the voids are considerably smaller and did not coalescence in comparison with other zones subjected to milder conditions. Hereafter, these observations are linked with the simulation results seeking for a coherence between the induced conditions and the void distribution within different radial zones and cores. As it will be shown, these crosschecks lead to the identification of relations between the void sizes, temperature and pressure ranges. And, in particular, certain temperature and pressure windows in which the void growth and coalescence seems to be enhanced.

Fig. 21 shows, for cores no. 2–9, the maximum temperature reached during pulse 25 as a function of the core radius. The voids were created and grew at temperatures close to these ones, since very little heat transfer takes place during the 50–100 μs duration of the dynamic response. The temperature has been plotted as a function of the radius

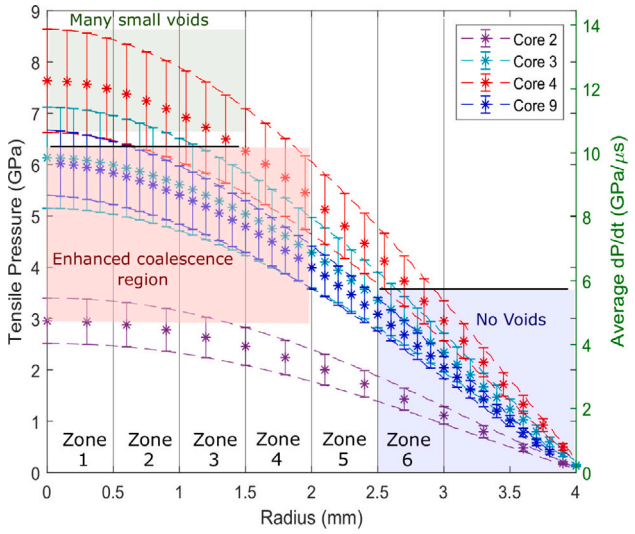

Fig. 22. Estimated maximum tensile pressure reached close to the longitudinal centre of cores 2-3-4-9 during pulse 25. These are reached during the second oscillation of the dynamic response. Right *Y*-axis represent the associated time average pressure rates. The error bars represent the variation within the cross-sections situated at ±2.5 mm with respect the longitudinally centred one.

in order to be crosschecked with the radial discretization of void distribution and porosity of Figs. 19 and 20. These values correspond to the ones reached in the cross-sections close to the longitudinal centre of the cores, where the maximums are reached. The error bars represent the variation in temperature within the cross-sections located at ±2.5 mm with respect the longitudinal centre, consistently with the ±0.5 mm uncertainty in the exact cutting and polishing position when slicing the cores. Similarly, Fig. 21 shows the maximum tensile pressure for cores no. 2, 3, 4 and 9 during pulse 25.[1] This maximum tensile pressure corresponds to the one reached during the second oscillation of the excited mode. The right *Y*-axis of the plot shows the time-averaged pressure rate (dP/dt) associated to the reached tensile pressure, which is obtained by simply dividing the pressure values by 0.69 μs (1/4 of the mode period). Higher instantaneous pressure rates are reached due to the sinusoidal nature of the load (up to 23 GPa/μs for the centre of core no. 4).

By crosschecking Figs. 21 and 22 with the void distribution of Fig. 19, one can identity certain coherence. For example, according to Fig. 21, the temperature range present during the dynamic response in the radial zones 1–4 for core no. 9 (1300–1800 °C) – where large voids were observed – coincides with the ones reached in zone 4 for cores no. 3–8. This is coherent with Fig. 19, where very large voids are observed in zones 1–4 for core no. 9, as well as relatively larger voids in zone 4 for cores no. 4–6 (following the "crown-like" distribution). A similar tendency can be observed for the maximum tensile pressure presented in Fig. 22. Following this approach three different pressure and temperature windows corresponding to the previously identified regions with common void distribution features have been found:

1. Window regime with no voids: areas exposed to temperatures below 1300 °C and maximum tensile pressures below 3 GPa (radial zones 6 and 7 for all the cores).

[1] Cores no. 5–8 have been left out plot for visual simplification. The maximum estimated tensile pressure reached in cores no. 5 and 6 are within 5% compared to the ones reached in core no. 4. For the case of core no. 7, the pressure response is between the one of cores no. 4 and 9.

2. Window regime in which growth and coalescence of voids is enhanced: areas exposed to the temperature window of 1300–1800 °C and tensile pressures in the range from 3 GPa to 6.3 GPa. The average pressure rates associated to this regime are within 5 and 10 GPa/μs. Average void diameter observed are within 250–400 μm.
3. Window regime in which growth and coalescence of voids is limited: areas exposed to the temperatures above 2000 °C and tensile pressures above 6.5 GPa. This corresponds to radial zones 1–2 for cores no. 4–6, where average voids diameter observed are within 18–40 μm.

These depicted temperature and pressure windows associated to each regime have to be considered as tendency estimates since the analysis presents some features that shall be taken into account: there is a limited number of sliced samples to provide extended statistics of void distribution, in addition to uncertainties in their exact cutting position as well as in the potential influence of the discretization in steps of 0.5 mm, which is arbitrary. The analysis considers that the potential pressure and temperature influence is uncoupled, which may not be the case. Furthermore, the estimated conditions correspond to a representative proton pulse impact (pulse 25), while in reality there were 47 pulses and in some of them, such as the last ones, the temperatures and tensile pressure reached were slightly higher (up to 2600–2700 °C). It is not possible to know which pulse impacts had a major contribution to the progressive void nucleation, growth and coalescence. Finally, the observed recrystallization in the central parts of cores 3–8 would lead to a different microstructure and hence a potential different material response to the same exposed tensile pressure. Nevertheless, despite all these uncertainties, Figs. 19–22 strongly suggest the fact that above a certain level of temperatures and/or tensile pressures, the process of voids coalescence and grow seems to be limited. This is the main message of the analysis.

5. Discussion of the results and conclusions

The HRMT-42 experiment exposed ten tantalum rods to 47 high energy (440 GeV/c momentum) proton pulse impacts. Each of these proton impacts induced a sudden rise of temperature in the bulk of such rods (referred as cores), with the subsequent excitation of a mode of vibration that exposed them to oscillating compressive-to-tensile pressures of several gigapascals. As demonstrated, this cyclic type of load presents very unique characteristics such as a high stress triaxiality, non-uniaxial plastic strain and high temperatures. In turn, each of the proton beam impacts induced a progressive heating of the cores leading to a range of maximum temperatures reached per pulse ranging from 1800 °C to 2700 °C. In addition, each of the cores as well as each radial position within them were exposed to different pressures and temperatures.

The appearance of voids in the bulk of the tantalum cores – attributed to a spalling process – motivated the detailed numerical characterization of the dynamic load that induced it. The results have shown that voids started to nucleate only in zones exposed to cyclic loading above 3 GPa. This is somehow consistent with previous experimental values reported in the literature, such as the 3.3 GPa onset for void nucleation in Ref. Roy (2003) or 4.4–4.6 GPa for spall strength at $8 \cdot 10^4$ s^{-1} reported in Ref. Antoun et al. (2003) (considering already void coalescence). However, these reported values correspond to tests performed close to room temperature, whereas in our experiment the temperatures in such voids-free areas were as high as 1300 °C. Nevertheless, it has been reported in the literature that for materials such as Cu or Mo the spall strength decreases very moderately when increasing temperature, especially in the range below $0.8T_{melting}$ (Antoun et al., 2003). Our observations could indicate that this moderate influence in this temperature range would apply also for tantalum.

Two different trends in the tantalum response have been identified above 1300 °C and 3.5 GPa: (i) Enhanced void growth and coalescence in the regime comprising 1300–1800 °C, tensile pressures from 3 GPa to 6.3 GPa, and average pressure rates from to 5 to 10 GPa/μs. (ii) Limited void growth in the range T>2000 °C, tensile pressures in the range of 6.5 GPa–9 GPa, and average pressure rates from 11 to 14 GPa/μs.

Four potential governing factors are presented to try to explain this trend and, in particular, why voids are smaller in the latter regime. First attempt could be related to the temperature. There is very limited information in the literature about spalling taking place at high temperatures. Only one report has been found, Ref. Bless and Paisley (1984), in which comparisons between flyer plate impacts on OFHC Copper at room temperature and 425 °C led to the observation of smaller and more isolated voids at high temperature, bringing the hypothesis of slower void growth at such conditions. Nevertheless, that study lacks an interpretation of such observation and, at the same time, reports that spall strength at elevated temperatures in Cu did not differ sufficiently to justify a temperature-dependent spall criterion.

A second attempt could be then related to the strain and pressure rates. Indeed, it is well known that tantalum spall strength increases with increasing strain rate. This has been reported both in many experiments such as in Refs. Razorenov et al. (2011), Ashitkov et al. (2015) and Hahn et al. (2017), as well as modelled through theoretical studies (Ref. Czarnota and S. Mercier, 2006). However, the measured change in strain-rate inducing a variation in the spall strength from 4 to 8 GPa is in the order of 30 times (Razorenov et al., 2011), whereas in our case the observed tendency change is associated to strain rates only 1.75 times higher. In addition, according to the model predicting void growth and coalescence in Ref. Czarnota et al. (2006), a change of the loading rate from 6 to 14 GPa/μs would imply only a 1.5 GPa increase in the spall pressure. For our case, however, the difference in tensile load between the zones with low and high voids coalescence was higher than this increase in strength. Finally, it is important to take into account that the pressure load was sinusoidal, and so was the pressure rate. This means in practice that the zones subjected to the highest pressure rates were also subjected during certain time to lower ones. Therefore, the pressure rate sensitivity would not explain why larger voids did not grow in such zones during this time. Stress triaxiality does not seem to be an explanation either, since as shown in Fig. 10, the load is still highly triaxial in the areas with larger voids.

Third governing factor could be then related to the different loading path in the zones. In particular, the influence that the compression phase during the load oscillations could have in the void growth. It has been reported in the literature that the asymmetries in the compression–tension behaviour of porous metals greatly influences the mechanisms of void growth (Revil-Baudard and Cazacu, 2013). This asymmetry, if present in tantalum at different temperatures, could imply that nucleated voids could close – or have a limited growth – in the central regions exposed to temperatures above 2100 °C during the compression part of the load, which reached up 8 GPa in compression. This could be enhanced by the high softening of Ta and such high temperatures. On the other hand, in the regions exposed to temperature ranges of 1300–1800 °C, a different tension–compression asymmetry could have enhanced void growth. In order to validate this hypothesis, the development of a more advanced material model would be necessary. Such development would require a systematic testing in tension and compression for both quasi-static and at high strain rates and temperatures (up to the strain-rates achievable with Split-Hopkinson). These model predictions may then be validated by conducting Taylor impact tests where gradients of pressures of the order of GPa are reached.

Finally, the fourth governing factor proposed is the potential influence on the microstructure and the observed full recrystallization in the central regions of cores 4–6 as shown in Figs. 15–16. The temperature–time plot of Fig. 5 indicated that such recrystallization

were temperature induced since, as shown by the in-situ EBSD measurements of Ref. Kerisit et al. (2013), incipient recrystallization can take place after annealing at 1030 °C for just 2 s. For instance, the temperature–time plot of Fig. 5 shows that the central regions of core no. 4 (where limited void growth took place) were exposed to temperatures well above 1600 °C for 4 s. It is well known that microstructure influences the spall strength since void nucleation and growth processes differ if the nucleation site is transgranular, intergranular, or close to a triple point (Llorca et al., 2000b; Remington et al., 2018; Cheng et al., 2018). These studies show higher void growth rates in intergranular voids (at grain boundaries) than in the intragranular ones, since these boundaries could act as heterogeneous nucleation sites for microvoids that nucleate and grow preferentially (Remington et al., 2018). Consequently, spall strength decreases with grain size in some regimes, following an inverse Hall–Petch behaviour (Wilkerson and Ramesh, 2016). Therefore, it could be thought that the zones in the cores subjected to higher temperatures (inducing recrystallization with the associated formation of new large grains) would provide less grain boundaries in comparison within the zones subjected to lower temperatures and remaining in non-annealed state (which presented extremely deformed grains). Hence, void growth would have been enhanced in the latter non-annealed zones as more grain boundaries would be available. This small difference in the void growth trend depending on the microstructure would have been particularly relevant due to the high number of loading cycles.

To conclude, the combination and variation of multiple variables (temperature, pressure rates, microstructure) present in the experiment complicates establishing a final explanation about the major governing factor within the ones discussed. Nevertheless, the main goal of the present study was to describe the conditions at which this phenomenon has taken place in terms of temperatures, flow stress and pressures and compare with post-experiment observations. The simulation models employed are relatively simple, considering the material as a continuous and not taking into account any void related process. In this context, a significant improvement would be to apply a more advanced modelling, taking into account porous plasticity, such as with a Gurson-type model (Gurson, 1977) or with its advanced extensions, considering porosity nucleation and coalescence. This advanced modelling, which is key to understand the mechanisms of void nucleation and growth, will be the scope of future works.

In addition, ongoing studies involving more samples and better statistics are being carried out to reinforce the conclusions. In this context, an additional experiment has been recently performed at the CERN's HiRadMat facility (named HRMT-48 PROTAD Torregrosa et al., 2019a). This experiment exposed more samples of different grades of tantalum (annealed/non-annealed) to similar conditions and a higher number of proton pulse impacts. Further examinations of these additional samples will provide more information to complete the proposed hypotheses.

Moreover, it is foreseen to execute post irradiation examination of an operational antiproton target after the 2021 operational run, which will allow to bridge the gap between tantalum irradiation in HiRadMat with some hundreds of proton pulses up to hundreds of thousands of pulses.

Declaration of competing interest

The authors declare that they have no known competing financial interests or personal relationships that could have appeared to influence the work reported in this paper.

Acknowledgements

The authors want to thank the CERN's Accelerator Consolidation (ACC-CONS) Project, which financed this work. In addition, the research leading to these results has received funding from the European Commission under the FP7 Research Infrastructures project EUCARD-2, Grant Agreement No. 312453.

References

2015. ASTM E407-07(2015)e1, Standard Practice for Microetching Metals and Alloys. Tech. rep., ASTM International, West Conshohocken, PA, URL http://www.astm.org/cgi-bin/resolver.cgi?E407-07(2015)e1.

Antoun, T., Curran, D., Seaman, L., Kanel, G., Razorenov, S., Utkin, A., 2003. Spall fracture. In: High pressure shock compression of condensed matter, Springer.

Ashitkov, S.I., Komarov, P.S., Struleva, E.V., Agranat, M.B., Kanel, G.I., Khishchenko, K.V., 2015. The behavior of tantalum under ultrashort loads induced by femtosecond laser. J. Phys. Conf. Ser. 653, 012001. http://dx.doi.org/10.1088/1742-6596/653/1/012001.

Bless, S.J., Paisley, D.L., 1984. Chapter IV : 3 - dynamic tensile fracture of ofhc copper. In: Asay, J., Graham, R., Straub, G. (Eds.), Shock Waves in Condensed Matter 1983. Elsevier, Amsterdam, pp. 163–166. http://dx.doi.org/10.1016/B978-0-444-86904-3.50038-5, URL http://www.sciencedirect.com/science/article/pii/B9780444869043500385.

Browning, P.N., Alagic, S., Carroll, B., Kulkarni, A., Matson, L., Singh, J., 2017. Room and ultrahigh temperature mechanical properties of field assisted sintered tantalum alloys. Mater. Sci. Eng. A 680, 141–151, URL http://www.sciencedirect.com/science/article/pii/S0921509316311480.

Chen, S., Gray III, G., Bingert, S., 1996. Mechanical Properties and Constitutive Relations for Tantalum and Tantalum Alloys Under High-Rate Deformation. Tech. Rep. LA-UR-96-0602, Los Alamos.

Cheng, M., Li, C., Tang, M., Lu, L., Li, Z., Luo, S., 2018. Intragranular void formation in shock-spalled tantalum: Mechanisms and governing factors. Acta Mater. 148 (J. Appl. Phys. 99 2006), 38–48. http://dx.doi.org/10.1016/j.actamat.2018.01.029, URL https://app.dimensions.ai/details/publication/pub.1100810549.

Czarnota, C., Mercier, S., Molinari, A., 2006. Modelling of nucleation and void growth in dynamic pressure loading, application to spall test on tantalum. Int. J. Fract. 141 (1), 177–194. http://dx.doi.org/10.1007/s10704-006-0070-y.

Czarnota, C., S. Mercier, A.M., 2006. Modelling of nucleation and void growth in dynamic pressure loading, application to spall test on tantalum. Int. J. Fract. 141 (1), 177–194. http://dx.doi.org/10.1007/s10704-006-0070-y.

Efthymiopoulos, I., Hessler, C., Gaillard, H., Grenier, D., Meddahi, M., Trilhe, P., Pardons, A., Theis, C., Charitonidis, N., Evrard, S., Vincke, H., Lazzaroni, M., 2011. HiRadMat: A new irradiation facility for material testing at CERN. In: Proceedings of IPAC2011. San Sebastián, Spain. pp. 1665–1667.

Ferrari, A., Sala, P., Fasso, A., Ranft, J., 2005. FLUKA: A Multi-Particle Transport Code. Tech. Rep., CERN, Geneva, Switzerland.

Fornasiere, E., 2020. Post-Irradiation Examination of Refractory Metal Candidates for Antiproton Targets at the European Laboratory for Particle Physics (CERN) (Ph.D. thesis). EPFL, Lausanne, p. 309. http://dx.doi.org/10.5075/epfl-thesis-7542.

Gurson, A.L., 1977. Continuum theory of ductile rupture by void nucleation and growth: Part I—Yield criteria and flow rules for porous ductile media. J. Eng. Mater. Technol. 99 (1), 2–15. http://dx.doi.org/10.1115/1.3443401.

Hahn, E.N., Germann, T.C., Ravelo, R., Hammerberg, J.E., Meyers, M.A., 2017. On the ultimate tensile strength of tantalum. Acta Mater. 126, 313–328. http://dx.doi.org/10.1016/j.actamat.2016.12.033.

Hopkinson, B., 1914. A method of measuring the pressure produced in the detonation of high explosives or by the impact of bullets. Phil. Trans. R. Soc. Lond. 213, 437.

Johnson, G., Cook, W., 1983. A constitutive model and data for metals subjected to large strains, high strain rates and high temperatures. The Hague, Netherlands.

Kerisit, C., Loge, R., Jacomet, S., Llorca, V., Bozzolo, N., 2013. EBSD coupled to SEM in situ annealing for assessing recrystallization and grain growth mechanisms in pure tantalum. J. Microsc. 250 (3), 189–199. http://dx.doi.org/10.1111/jmi.12034, URL https://onlinelibrary.wiley.com/doi/abs/10.1111/jmi.12034.

Llorca, F., Roy, G., Antoine, P., 2000a. Ductile damage of tantalum under spalling effects. experimental and metallurgical analysis. J. Phys. IV 10, 775.

Llorca, F., Roy, G., Antoine, P., 2000b. Ductile damage of tantalum under spalling effects. experimental and metallurgical analysis. J. Phys. IV France 10 (Pr9), 775–780. http://dx.doi.org/10.1051/jp4:20009128.

Meyers, M., Aimone, C., 1983. Dynamic fracture (spalling) of metals. Prog. Mater. Sci. 28 (1), 1–96. http://dx.doi.org/10.1016/0079-6425(83)90003-8, URL http://www.sciencedirect.com/science/article/pii/0079642583900038.

Molinari, A., Mercier, S., Jacques, N., 2014. Dynamic failure of ductile materials. Procedia IUTAM 10, 201–220. http://dx.doi.org/10.1016/j.piutam.2014.01.019, Mechanics for the World: Proceedings of the 23rd International Congress of Theoretical and Applied Mechanics, ICTAM2012. URL http://www.sciencedirect.com/science/article/pii/S2210983814000200.

Obererlacher, A., 2014. Product Specification TaM Rod. Tech. Rep. PS-MPR-112, Plansee.

Razorenov, S., Garkushin, G., Kanel, G., Ignatova, O., 2011. The spall strength and hugoniot elastic limit of tantalum with various grain size. In: APS Shock Compression of Condensed Matter Meeting Abstracts. p. CKJ.10.

Remington, T., Hahn, E., Zhao, S., Flanagan, R., Mertens, J., Sabbaghianrad, S., Langdon, T., Wehrenberg, C., Maddox, B., Swift, D., Remington, B., Chawla, N., Meyers, M., 2018. Spall strength dependence on grain size and strain rate in tantalum. Acta Mater. 158, 313–329. http://dx.doi.org/10.1016/j.actamat.2018.07.048, URL http://www.sciencedirect.com/science/article/pii/S1359645418305846.

Remington, T.P., Remington, B.A., Hahn, E.N., Meyers, M.A., 2017. Deformation and failure in extreme regimes by high-energy pulsed lasers: A review. Mater. Sci. Eng. A 688, 429–458. http://dx.doi.org/10.1016/j.msea.2017.01.114, URL http://www.sciencedirect.com/science/article/pii/S092150931730148X.

Revil-Baudard, B., Cazacu, O., 2013. On the effect of the matrix tension–compression asymmetry on damage evolution in porous plastic solids. Eur. J. Mech. A Solids 37, 35–44. http://dx.doi.org/10.1016/j.euromechsol.2012.05.001, URL http://www.sciencedirect.com/science/article/pii/S0997753812000605.

Rohsenow, W.M., Hartnet, J.P., Cho, Y.I., 1998. Handbook of Heat Transfer. McGraw-Hill Education.

Roy, G., 2003. Vers Une Modelisation Approfondie De L'endommagement Ductile Dynamique: Investigation Experimentale D'une Nuance De Tantale Et Developpements Theoriques (Ph.D. thesis). Ecole Nationale Superieure de Mecanique et d Aeronautique, Universite de Poitiers.

Solieri, N., 2017. Dynamic Studies of Multiple Configurations of CERN Antiproton Decelerator Target Core Under Proton Beam Impact (Master's thesis). URL https://cds.cern.ch/record/2310189.

Steinberg, D.J., 1996. Equation of State and Strength Properties of Selected Materials. Lawrence Livermore National Laboratory.

Thissell, W., Tonks, D., Schwartz, D., House, J., 2003. Dynamic failure resistance of two tantalum materials with different melt practice sequences. Shock Compress. Condens. Matter 706, 495.

Torregrosa, C., 2018. Comprehensive Study for an Optimized Redesign of the CERN's Antiproton Decelerator Target (Ph.D. thesis). Universidad Politecnica de Valencia, URL https://cds.cern.ch/record/2314375/files/CERN-THESIS-2017-357.pdf.

Torregrosa, C., Calviani, M., Perillo-Marcone, A., Ferriere, R., Solieri, N., Grec, L.-M., Butcher, M., Canhoto, J., 2018. Scaled prototype of a tantalum target embedded in expanded graphite for antiproton production: Design, manufacturing, and testing under proton beam impacts. Phys. Rev. Accel. Beams 21, 073001, URL https://link.aps.org/doi/10.1103/PhysRevAccelBeams.21.073001.

Torregrosa, C., Calviani, M., Solieri, N., Canhoto, J., Perillo-Marcone, A., Ferriere, R., Fornasiere, E., Busom, J., Dickinson, B., 2019a. First prototypes of the new design of the CERN's antiproton production target. Mater. Des. Process. Commun. 1 (2), e38. http://dx.doi.org/10.1002/mdp2.38, URL https://onlinelibrary.wiley.com/doi/abs/10.1002/mdp2.38.

Torregrosa, C., Perillo-Marcone, A., Calviani, M., Gentini, L., Butcher, M., Munoz-Cobo, J.-L., 2019b. Experiment exposing refractory metals to impacts of 440 gev/c proton beams for the future design of the CERN antiproton production target: Experiment design and online results. Phys. Rev. Accel. Beams 22, 013401. http://dx.doi.org/10.1103/PhysRevAccelBeams.22.013401, URL https://link.aps.org/doi/10.1103/PhysRevAccelBeams.22.013401.

Torregrosa, C., Perillo-Marcone, A., Calviani, M., Munoz-Cobo, J.-L., 2016. CERN antiproton target: Hydrocode analysis of its core material dynamic response under proton beam impact. Phys. Rev. Accel. Beams 19, 073402. http://dx.doi.org/10.1103/PhysRevAccelBeams.19.073402, URL https://link.aps.org/doi/10.1103/PhysRevAccelBeams.19.073402.

Wilkerson, J.W., Ramesh, K.T., 2016. Unraveling the anomalous grain size dependence of cavitation. Phys. Rev. Lett. 117, 215503. http://dx.doi.org/10.1103/PhysRevLett.117.215503, URL https://link.aps.org/doi/10.1103/PhysRevLett.117.215503.

Zerilli, F., Armstrong, R., 1987. Dislocation-mechanics-based constitutive relations for material dynamics calculations. J. Appl. Phys. 61, 1816.

Zurek, A., Gray III, G., 1996. Constitutive behavior of tantalum and tantalum-tungsten alloys. Metall. Trans. A 27 (A), 2994–3006.

Zurek, A., Thissell, W., Johnson, J., Tonks, D., Hixson, R., 1996. Micromechanics of spall and damage in tantalum. J. Mater Process. Technol. 60 (1), 261–267.